metals

MDPI

Article

Structure, Texture and Phases in 3D Printed IN718 Alloy Subjected to Homogenization and HIP Treatments

Ahmad Mostafa [1], Ignacio Picazo Rubio [1], Vladimir Brailovski [2], Mohammad Jahazi [2] and Mamoun Medraj [1,3,*]

[1] Mechanical and Materials Engineering Department, Khalifa University of Science and Technology, Masdar Institute, P.O. Box 54224 Abu Dhabi, UAE; a.mostafa@concordia.ca (A.M.); ignacio.picazo.rubio@gmail.com (I.P.R.)

[2] Department of Mechanical Engineering, École de Technologie Supérieure, 1100, Notre-Dame Street West, Montreal, QC H3C 1K3, Canada; vladimir.brailovski@etsmtl.ca (V.B.); mohammad.jahazi@etsmtl.ca (M.J.)

[3] Mechanical Engineering Department, Concordia University, 15151 Rue Sainte Catherine west, Montreal, QC H3G 2W1, Canada

* Correspondence: mmedraj@encs.concordia.ca; Tel.: +1-514-848-2424

Academic Editor: Johannes Henrich Schleifenbaum
Received: 11 April 2017; Accepted: 19 May 2017; Published: 30 May 2017

Abstract: 3D printing results in anisotropy in the microstructure and mechanical properties. The focus of this study is to investigate the structure, texture and phase evolution of the as-printed and heat treated IN718 superalloy. Cylindrical specimens, printed by powder-bed additive manufacturing technique, were subjected to two post-treatments: homogenization (1100 °C, 1 h, furnace cooling) and hot isostatic pressing (HIP) (1160 °C, 100 MPa, 4 h, furnace cooling). The Selective laser melting (SLM) printed microstructure exhibited a columnar architecture, parallel to the building direction, due to the heat flow towards negative *z*-direction. Whereas, a unique structural morphology was observed in the *x*-*y* plane due to different cooling rates resulting from laser beam overlapping. Post-processing treatments reorganized the columnar structure of a strong {002} texture into fine columnar and/or equiaxed grains of random orientations. Equiaxed structure of about 150 μm average grain size, was achieved after homogenization and HIP treatments. Both δ-phase and MC-type brittle carbides, having rough morphologies, were formed at the grain boundaries. Delta-phase formed due to γ″-phase dissolution in the γ matrix, while MC-type carbides nucleates grew by diffusion of solute atoms. The presence of $(Nb_{0.78}Ti_{0.22})C$ carbide phase, with an fcc structure having a lattice parameter a = 4.43 Å, was revealed using Energy dispersive spectrometer (EDS) and X-ray diffractometer (XRD) analysis. The solidification behavior of IN718 alloy was described to elucidate the evolution of different phases during selective laser melting and post-processing heat treatments of IN718.

Keywords: Inconel 718; additive manufacturing; 3D printing; hot isostatic pressing (HIP); homogenization treatment; selective laser melting (SLM); Electron backscattered diffraction (EBSD)

1. Introduction

Selective laser melting (SLM) process is the most widely used process for additive manufacturing (AM) of complex and customized parts in different industries, such as aerospace and automotive sectors and in the medical field [1]. In this method, laser beam selectively melts the surface of a metallic powder to create a fully-dense (close to 99.7%) solid structures with mechanical properties comparable to those achieved by wrought or casting processes, depending on the initial powder composition and process parameters [1,2]. Besides the design freedom capabilities, the reduced manufacturing time and

possibility to fabricate large number of parts without necessarily using other supplementary processes are other important advantages of SLM process over conventional manufacturing methods [1,3].

Nickel-iron based superalloys are widely used in applications that require remarkably high strength and high corrosion resistance at elevated temperatures, such as jet engine components, aerospace parts, and fossil fuel and nuclear power plant components [4,5]. Among nickel-iron superalloys family, IN718 stands out for its excellent mechanical properties and good corrosion resistance at elevated temperatures, up to 650 °C, making it the most extensively used superalloy [2,6].

To date, there have been several studies on SLM processing of nickel-iron based superalloys [7–15]. Jia and Gu [13] investigated the densification behavior, microhardness, microstructural features, high-temperature oxidation properties and wear performance of IN718 parts fabricated by SLM. According to them, columnar grains growing parallel to the deposition direction, similar to those reported by other authors [16,17], were observed in the microstructure of as-printed SLM specimens. Furthermore, they [13] reported successive morphological changes by varying the applied laser energy density, such as clustered-coarse and uniformly distributed slender columnar dendrites. In the same line, Parimi et al. [18] investigated the variation in the deposition path and the laser power on the texture, grain structures and morphology development of different phases using unidirectional versus bidirectional building strategies [18]. In both strategies, columnar grains oriented along the moving heat source were produced. Laves phase, $(Ni,Cr,Fe)_2(Nb,Mo,Ti)$, carbides and the orthorhombic Ni_3Nb δ–phase precipitates were also detected in all fabricated specimens [18]. According to Wei et al. [19], the columnar grain growth epitaxial to the surface depends on the local temperature field near the growth interface and grain orientation of the substrate. The high power density, low laser power and high scanning speed were claimed to be beneficial for the columnar grain growth [19]. The columnar grain structure reported in all the above investigations, was found responsible for anisotropy in mechanical properties of components manufactured using laser additive manufacturing [20]. Wang et al. [16] investigated the influence of solution treatment (980 °C, 1 h, air cooling) followed by double aging (710 °C, 8 h, furnace cooling and 620 °C, air cooling) on the microstructure and tensile properties of IN718 specimens fabricated by SLM. The fabricated specimens showed dendritic microstructure with columnar grains, good metallurgical bonding and minimal porosity [16]. As a result of heat treatment, γ′-$Ni_3(Al,Ti,Nb)$ and γ″ (bct-Ni_3Nb) phases dissolved in the γ matrix (Ni-Cr solid solution) and the needle-like δ-phase formed at the grain boundaries. The tensile properties of the heat treated SLM-printed specimens were found comparable to those of the wrought IN718 alloys. The influence of hot isostatic pressing on the microstructure of IN718 fabricated by SLM was investigated by Amato et al. [17]. The HIP-treated microstructures showed more pronounced columnar γ″ precipitates with partially "recrystallized" structure [17]. Whereas, the microstructure of annealed specimens (1160 °C, 4 h) showed ~50% "recrystallized" structure with spheroidal γ′ precipitates distributed in a dense field of fine γ″ precipitates [17]. It is worth emphasizing that Amato et al. [17] used the term "recrystallization" to describe the change from dendritic to equiaxed structure.

Although many aspects of SLM manufacturing of IN718 have been investigated, information on suitable post-manufacturing procedures to improve the microstructure and reduce the inherent anisotropy is still needed. In the present work, the microstructural changes of the SLM-printed IN718 have been evaluated. This includes the changes in the microstructure, texture, and phases related to the printing process, the high temperature homogenization and, hot isostatic pressing (HIP) post-processing treatments. The generation of such information is a critical tool for the optimized design of the SLM process of superalloys as well as identification of the critical information on mechanical properties of SLM manufactured parts.

2. Materials and Methods

The starting material in the SLM experiments was gas atomized (GA) IN718 powder, supplied by EOS-GmbH (Krailling, Germany) [21], with an average particle size of 30 µm. The chemical composition of this powder is listed in Table 1.

Table 1. The chemical composition of as-received IN718 powder.

Element	wt %	Comments
Ni	52.7	Based on the analysis of the current work
Fe	18.5	
Cr	20.0	
Nb	4.8	
Mo	2.9	
Ti	1.1	
Al	0.45	
Co	≤1.0	Composition of trace elements as reported by [21]
Cu	≤0.3	
C	≤0.08	
Si, Mn	Each ≤ 0.35	
P, S	Each ≤ 0.015	
B	≤0.006	

Figure 1a is an SEM (Scanning electron microscope) image showing the particle size range. Most of the powder particles have spherical shape. However this shape might become irregular due to the partially fused small particles, known as satellites, which are attached to bigger particles during the gas atomizing process [18]. A high magnification secondary electron (SE) image of a satellite particle is shown in Figure 1b.

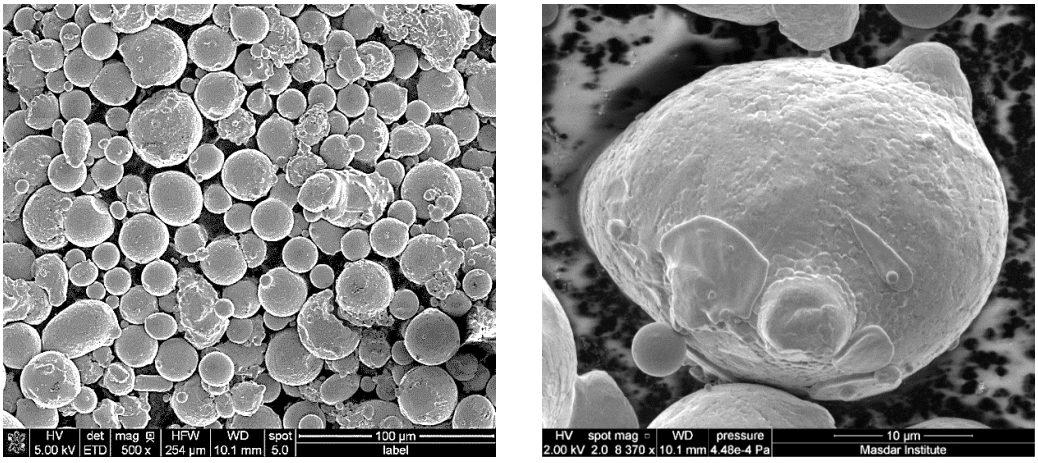

(**a**) (**b**)

Figure 1. (**a**) The as-received gas atomized IN718 powder showing the range of powder sizes; (**b**) magnified particle showing attached satellites.

Cylindrical specimens were fabricated in a powder bed, on a manufacturing platform, using an EOS M280 400 W (EOS, Krailling, Germany) Yb: YAG fiber laser system with PSW3.6 and Parameter Set IN718_Performace 1.0 (40 µm layer thickness, 100 µm laser beam diameter and 1000 mm/s scanning speed). The platform was preheated to 80 °C and maintained at that temperature to reduce thermal gradient between the fabricated part and the platform [17,22]. The cylindrical specimens, measuring 12 mm in diameter and 20 mm in length, were printed horizontally as shown in Figure 2a,

under nitrogen gas environment. A sketch of printing orientation and the actual printed specimen are shown in Figure 2a,b, respectively. The (x, y, z) coordination system used throughout the paper is demonstrated in Figure 2a. Scanning strategy refers to the path, which the laser beam follows during scanning of one layer and the angle between the layers. As illustrated in Figure 2c, in this work, bidirectional laser tracks were performed in one layer whilst the consecutive layers were turned 67° with respect to one another (i.e., hatch angle of 67°).

The post-fabrication heat treatment temperatures were chosen based on the transformation-time-temperature (TTT) diagram for IN718 welds [23], shown in Figure 3, to possibly dissolve the secondary phases and obtain homogeneous microstructure. TTT diagram of 3D printed IN718 could be found in the literature. The TTT diagram of IN718 welds is found suitable to describe the phase changes under rapid solidification conditions and hence is adopted in this work. The fabricated specimens were then subjected to a homogenization treatment at 1100 °C (1 h) under argon then furnace-cooled to room temperature. Some of the homogenized specimens were also subjected to hot isostatic pressing (HIP) treatment (1160 °C, 100 MPa, 4 h, under argon) followed by furnace cooling.

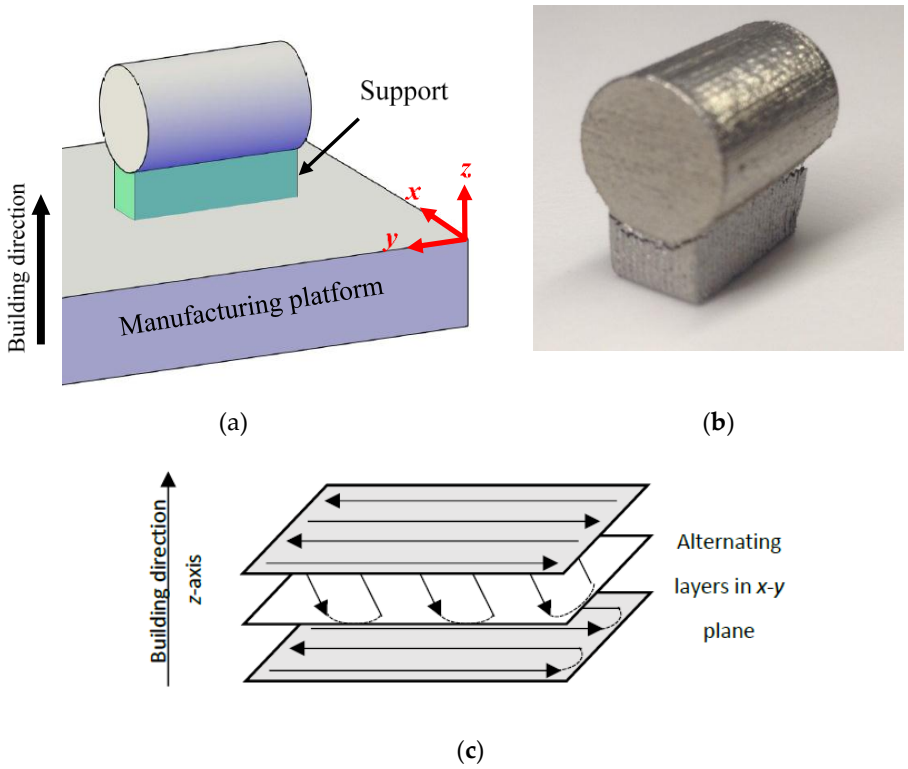

Figure 2. (**a**) Illustration of the cylindrical specimens manufactured in horizontal orientation with respect to the building direction; (**b**) actual printed specimen; (**c**) schematic illustration of the laser scanning strategy used in the current work.

Specimens representing the different conditions were cut into parallel and perpendicular cross sections, with respect to the building direction, using a slow cutter in a mineral oil bath to eliminate heat generation. Sectioned specimens were mounted in a hot-setting epoxy resin for metallographic sample preparation. The surfaces of the mounted specimens were ground gradually, up to 1200 grit SiC papers. Water was used as lubricant and coolant during grinding. The ground specimens were polished down to 0.25 µm using alcohol-based alumina suspension. A waterless Kalling's solution (5 g of $CuCl_2$, 100 cc of HCl and 100 cc of ethyl alcohol) with an etching time of 20–30 s, depending on the processing conditions, was found to be the most effective solution for revealing the microstructure of the current SLM manufactured specimens.

The microstructures of all specimens were observed by an Olympus BX51M optical microscope (Olympus, Tokyo, Japan) equipped with a digital camera. An FEI Quanta 250 field emission gun scanning electron microscope (FEG-SEM, FEI, Hillsboro, OR, USA), equipped with an energy dispersive X-ray spectrometer (EDS, EDAX Inc., Mahwah, NJ, USA) and an HKL electron backscattered diffraction (EBSD) detector (EDAX Inc., Mahwah, NJ, USA) was used for microstructural analysis. The SEM images, EDS chemical analysis and elemental mapping, were carried out at 20 keV and 4.5 spot size. The EDS detector was calibrated using reference peaks of pure Al and Cu. The chemical analyses were carried out using semi-quantitative EDS measurements. The uncertainty in the EDS measurements is addressed in the results section. A Panalytical Empyrean X-ray diffractometer (XRD, Spectris plc, Almelo, The Netherlands), using a Cu target, was utilized to identify the phases in powder and bulk specimens of different conditions. The XRD analyses were also carried out to determine the crystallographic grain orientations of the bulk specimens. The X-ray patterns were refined using Rietveld analysis in the X'pert Highscore software (Ver 3.0.2, PANalytical, Almelo, The Netherlands, 2011) [24]. Standard X-ray patterns, used to analyze the experimental data, were taken from Pearson's crystal database [25]. It is worth noting that structure, texture and phase analyses were performed at the center of the circular sections of printed and post-treated cylinders for concise comparison.

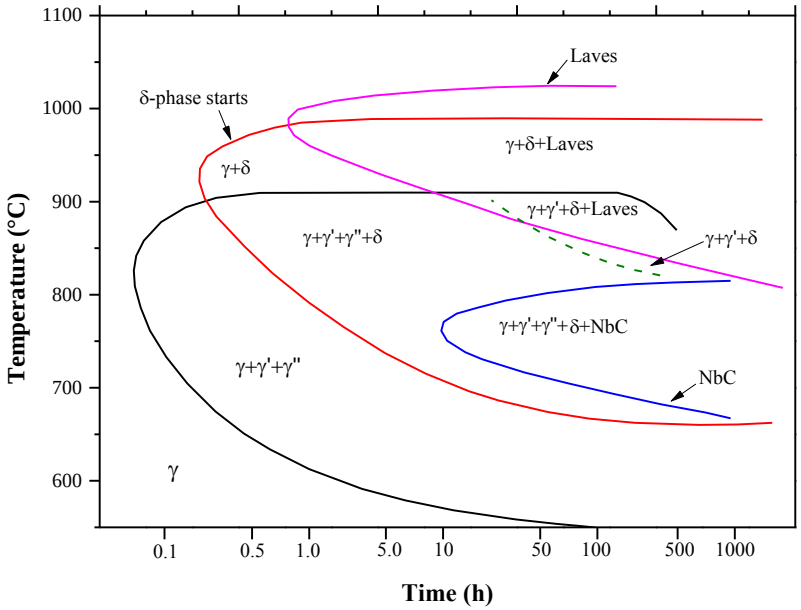

Figure 3. Transformation-time-temperature diagram of IN718 alloy system. Reproduced with the permission from [23]. Copyright American Welding Society, 1986.

3. Results and Discussion

3.1. Microstructural Characterization

3.1.1. Microstructure of the as-Received Powder

The surface morphology of a non-etched gas atomized particle and microdendritic structure of a mounted, sectioned and polished IN718 powder specimen are shown in Figure 4a,b, respectively. Figure 4a demonstrates the powder particles that are mostly spherical with very fine dendritic networks. This network might be a result of the rapid solidification, with a cooling rate of about 100 °C/s [26], during gas atomization process [18,27]. Non-etched powder particles were sectioned and imaged in Figure 4b to perform phase analysis. Almost no internal porosity could be observed in the sectioned powder particles.

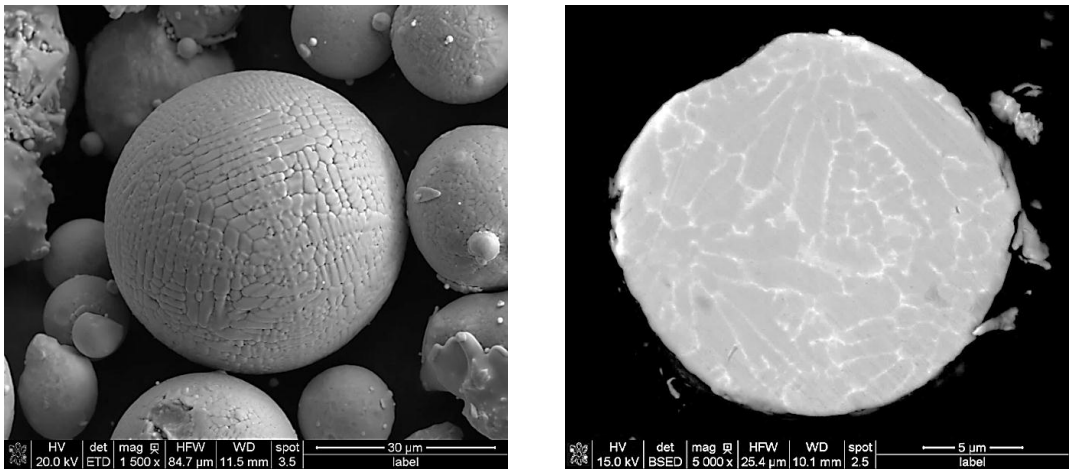

(**a**) (**b**)

Figure 4. (**a**) Backscattered electron (BSE) image showing the powder surface morphology; (**b**) BSE image of a mounted, sectioned and polished IN718 powder particle showing the internal microdendritic structure.

Elemental mapping of a sectioned IN718 powder particle, shown in Figure 5, was carried out using EDS analysis to determine the chemical composition of the microdendrites (grey phase) and the interdendritic spaces (white phase). The semi-quantitative elemental analysis revealed that the concentrations of Nb, Mo and Ti were higher in the interdendritic spaces than in the primary dendrites. On the other hand, Cr, Fe and Ni concentrations were found to be lower in the interdendritic spaces. Table 2 compares the chemical composition of the microdendrites and the interdendritic spaces obtained by the EDS analysis.

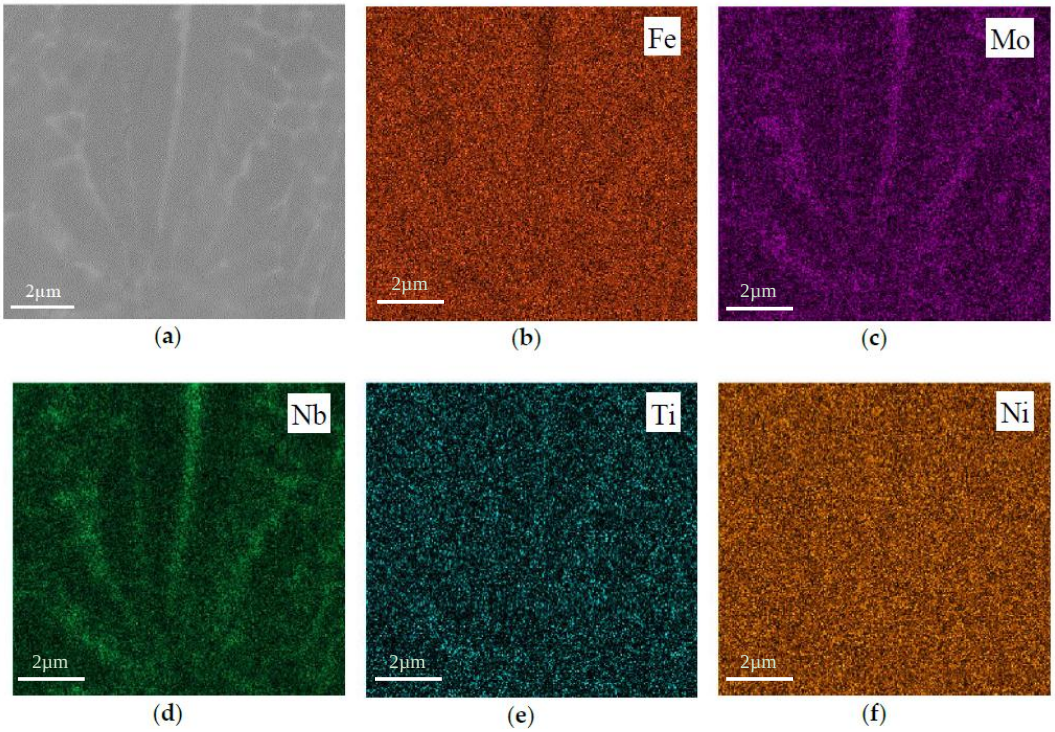

Figure 5. Energy dispersive spectrometer (EDS) elemental mapping of the sectioned IN718 powder particle shown in (**a**); (**b**–**f**) the elemental maps of Fe, Mo, Nb, Ti and Ni, respectively.

Table 2. Compositions of different phases observed in IN718 powder particles.

Element	Microdendrites		Interdendritic Spaces		EDS Error %
	wt %	at %	wt %	at %	
Nb	4.12	4.73	8.77	9.82	6.7
Mo	2.07	2.20	2.88	2.99	8.8
Ti	0.81	1.20	1.39	2.08	9.5
Cr	18.57	23.04	18.15	22.60	3.2
Fe	18.03	19.00	15.52	16.36	4.0
Ni	54.03	46.21	50.77	43.16	3.0
Trace	Balance	Balance	Balance	Balance	-

The XRD diagram of the phases in the starting IN718 GA powder reported in Figure 6 revealed the presence of the Ni-Cr solid solution (γ-phase) and the bct-Ni_3Nb, γ″-phase. Rietveld analysis was carried out using standard patterns #534317 for γ-phase and #1908308 for γ″-phase from Pearson's Crystal Database [25]. The volume fractions of these two phases were found to be about 85% and 15%, respectively. This big difference in the volume fraction was due to acquiring strong γ-phase signals from the powder surface and not from the interior structure. The X-ray pattern refinement was very challenging, because of the overlapping between the peaks of both phases and low quantity of γ″-phase (~15 vol %). However, the white phase in the interdendritic space regions was recognized as γ″-phase based on the current semi-quantitative EDS analysis and XRD refinements and from the available literature data [4,17,28]. No other phases, that are commonly associated with IN718 alloy such as γ′, carbides and Laves phase, could be detected in the starting powder. This is consistent with the results obtained by Amato et al. [17] for IN718 and by Murr et al. [4] for IN625.

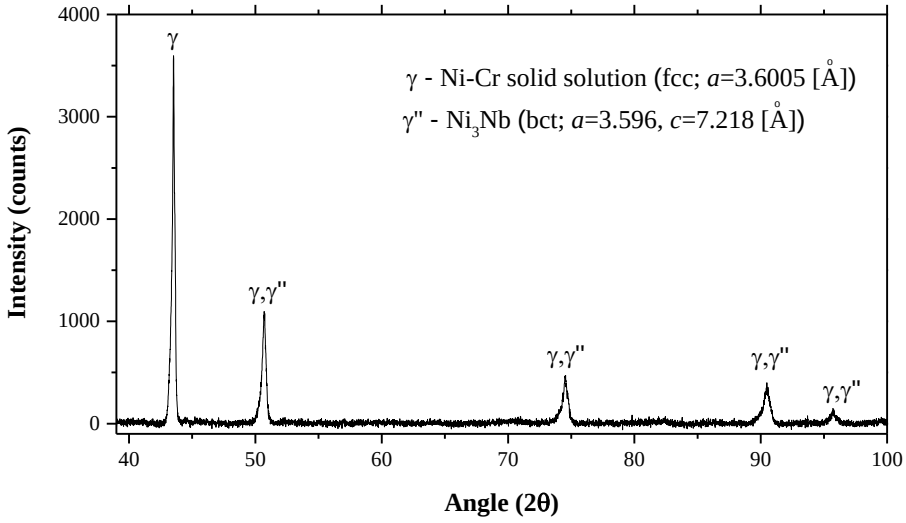

Figure 6. X-ray diffractometer (XRD) spectrum for the IN718 powder sample.

3.1.2. Microstructure of the as SLM-Printed Specimens

Figure 7 demonstrates the melt pool morphology near the substrate layers and on the top deposited layers. The near substrate region shows a Gaussian melt pool morphology with a structure containing fine columnar grains of small dendritic arm spacing, while the melt pool morphology near the top layers is significantly different. It shows almost flat boundaries in a layered fashion and contains columnar grains of large dendritic arm spacing. Such a morphology describes the multi-pass melting with significant overlapping in horizontal and vertical planes. The horizontal and vertical laser interactions, whose analogy is described in Figure 8, were the main reasons for varying the cooling rate between initial and final printed layers. The horizontal interactions are normally described by

percentage of laser beam overlapping in the *x*-*y* plane; whereas, the vertical overlapping is described by the layer thickness and hatch angle. The change in melt pool morphology and microstructure was attributed to the steep thermal gradient between the older and newer deposited layers during SLM process [15]. Also, Figure 7 indicates that the cooling rate is higher near the substrate than at the top of the cylinder. Amine et al. [29] estimated the cooling rates between the newly and previously deposited stainless steel layers, fabricated by laser melting deposition (LMD) process, to be ranging from 200 to 5500 °C/s. Good metallurgical bonding between new and old deposited layers that can be seen in Figure 7 indicates that the instantaneous thermal energy generated from laser power was not only enough to melt the IN718 powder above its melting temperature (1340–1364 °C [30]), but it was also high enough to melt the previously solidified layers.

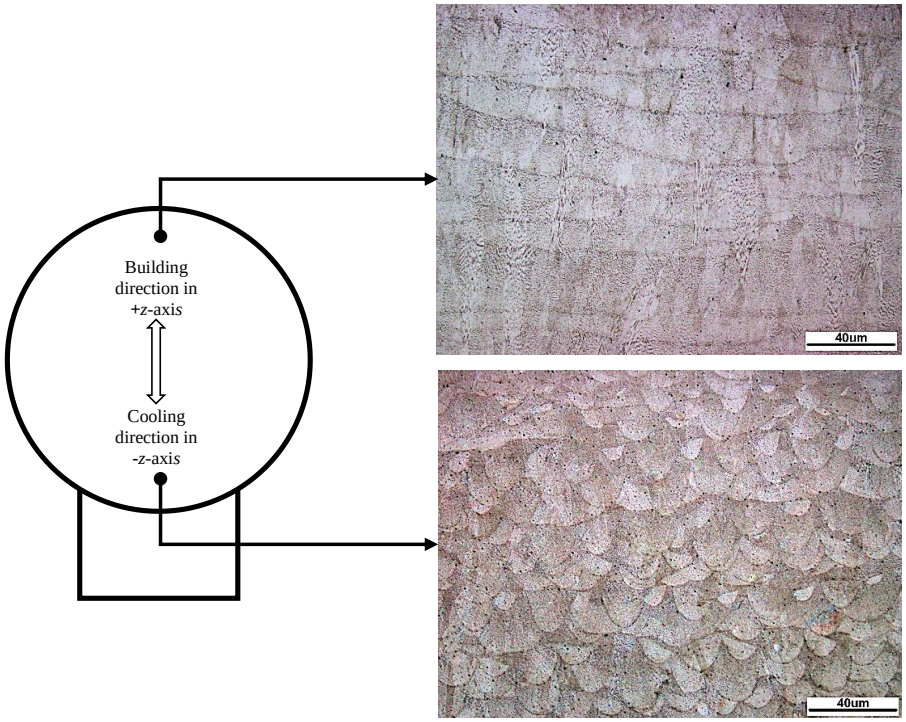

Figure 7. Melt pool morphology with reference to the SLM-printed cylinder, for both top and near substrate deposited layers.

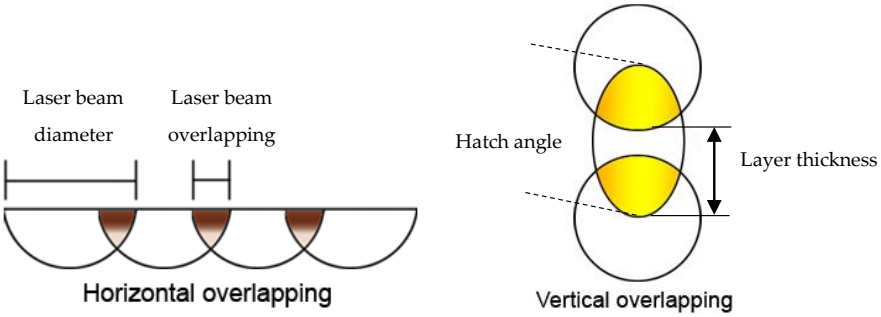

Figure 8. Illustration of vertical and horizontal laser overlapping.

Figure 9a shows the structure of the as SLM-printed IN718 alloy in the center of the cylindrical specimen. A layered disposition of the solidified material can be observed, which is also in agreement with that reported by other researchers [16,18,20]. The selected surface for analysis, with respect to the building direction, is illustrated in the lower right-hand-side corner. The melting pool boundaries

are almost parallel. The average thickness of the deposited layers in the center of the cylinder was measured to be about 40 μm. This thickness represents the actual size of the melting pool. It has been reported that the size and shape of the melting pool are mainly governed by the laser parameters (power, travel speed and beam diameter) and scanning strategy (hatch angle and hatch distance parameters) [2,29]. For example, Amine et al. [29] described the influence of the laser parameters on the size and shape of the melt pool, by means of the laser specific energy. Although the laser parameters were not changed in the course of this work, the shape and size of the melt pool have dramatically changed. This was strongly attributed to numerous reheating cycles exerted by the deposition and remelting of new layers over the old ones, which create a steep thermal gradient along the vertical axis of the SLM-built.

In addition to the melting pool boundary lines, the SLM-printed microstructure exhibited columnar grains growing parallel to the building direction. Figure 9b is a high magnification SE image of the microstructure of a columnar grain shown in Figure 9a. The columnar grain is composed of an array of microdendrites with similar orientations to the growth direction. Figure 9c shows the solidified microstructure in the vertical direction, which contains columnar grains parallel to the building direction. Figure 9d is a magnified image showing continuous grain growth across the melt pool boundary line.

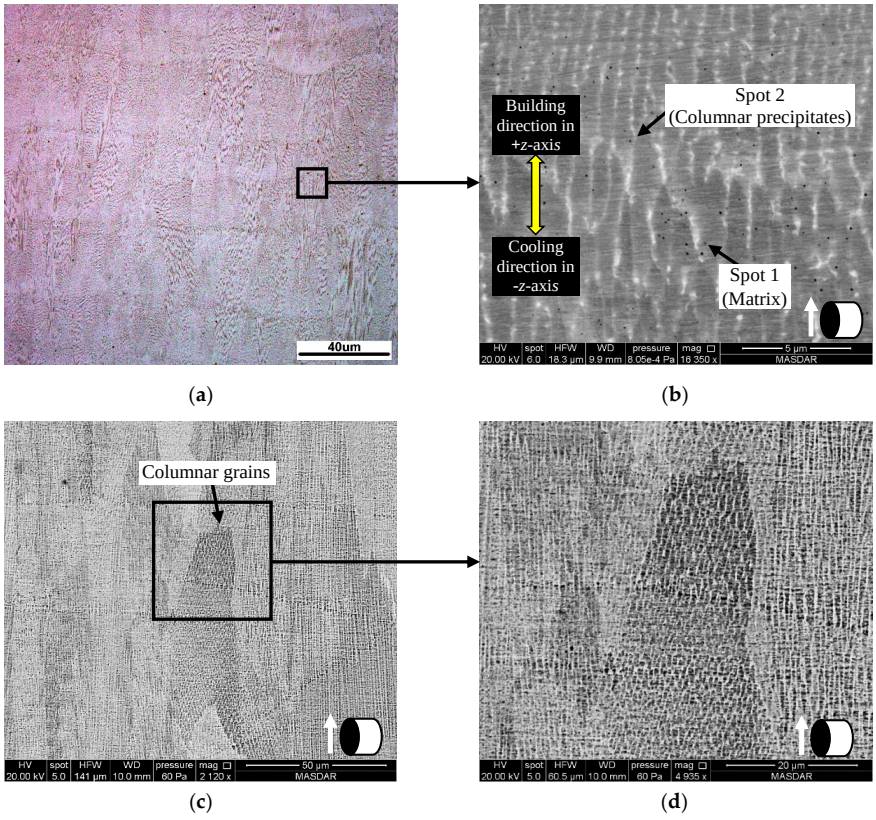

Figure 9. (**a**) Optical microscope images of the layer-by-layer structure of SLM process; (**b**) high magnification Scanning electron microscope (SEM) image of columnar micro-dendrites; (**c**,**d**) SEM micrographs showing a columnar grain continuously grew across the melting pool boundary.

The influence of the temperature gradient and solidification orientation on the microstructure of the specimens in the *x*-*y* plane (the perpendicular plane to the building direction as indicated schematically in the lower right-hand corner) is shown in Figure 10. The *x*-*y* section was taken at the center of the SLM-built cylinder in order to reduce the effect of structure inhomogeneity and to ensure the presence of a horizontal overlapping between the laser tracks. To achieve a desired section in

a single layer, a DNM-400 CNC milling machine (Doosan Machine Tools Co. Ltd., Seoul, Korea) was used to cut a perfectly horizontal surface (within the long side of the cylinder). The support block, attached to the SLM-printed specimen, was used as a reference for flat cutting. In this figure, the cross section of the columnar architecture showed various dendritic arm spacing and grain sizes in regions labeled as Zones I and II. The morphological differences between these zones stem from the variation in the cooling rates resulting from laser tracks overlapping during the 3D printing process. Similar morphological differences were observed by Vrancken et al. [31], who reported a thermal gradient between the midline and edge of a scan track due to laser beam overlapping. Choi et al. [15] studied the grain orientation in the *x*-*y* plane of an SLM-built IN718 alloy using optical microscopy and EBSD analysis. Accordingly, small equiaxed grains of around 10 µm average size were seen around the melt pool boundaries and their formation was referred to the grain partial melting due to laser track overlapping and/or presence of impurities [15].

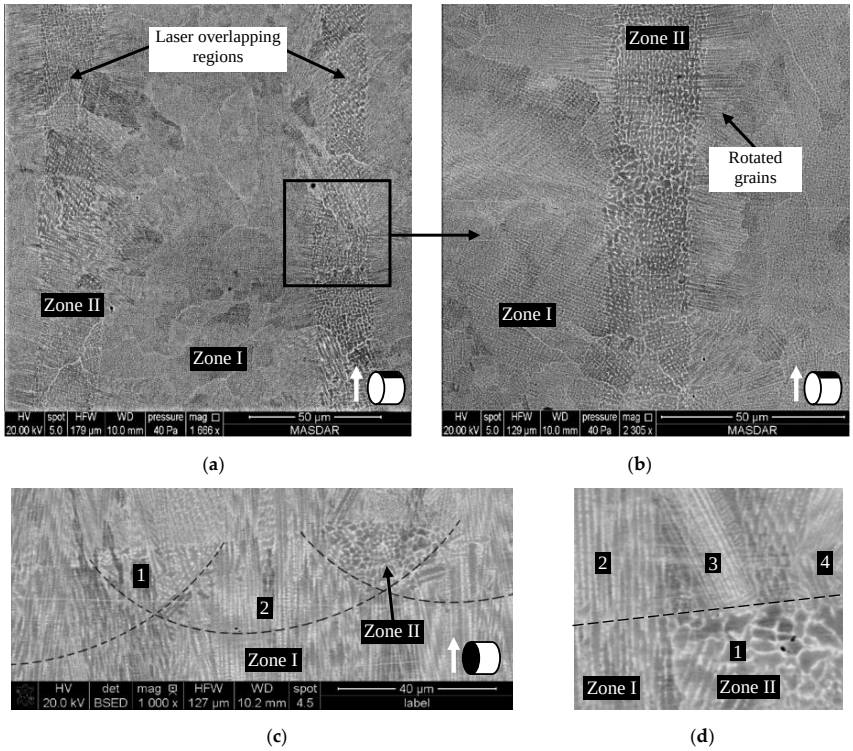

Figure 10. (**a**) SEM micrographs of the overlapping laser tracks microstructure in the *x*-*y* plane, with respect to the building direction *z*-axis (indicated with an arrow in the right low corner); (**b**) magnified image of one laser overlapping region; (**c**,**d**) cross section of laser overlapping region.

Zone I is located within the laser track area and shows finer dendrites of ~0.6 µm arm spacing and smaller grains of 30 µm average diameter as compared to ~1.25 µm arm spacing and 50 µm average grain diameter in Zone II that is located within the laser overlapping region. It is expected that the heat content in the laser overlapping region (Zone II) is higher than that in the laser track area (Zone I), because it falls within the laser double-pass region of the same layer. Whereas, Zone I falls within a laser single-pass of the same layer, where the heat dissipation is expected to be faster than that in Zone II. The slower cooling rate in Zone II is probably at the origin of the formation of rotated columnar grains [31] with large dendritic structure as indicated in Figure 10b. It is worth noting that, the width of the laser track is about 100 µm, which corresponds to the used laser spot diameter. Although Vrancken et al. [31] reported different microstructures and grain orientations due to thermal gradient, the periodic morphological features such as Zone I and Zone II (Figure 10) have not been reported in their work.

In an attempt to better understand the occurrence of the laser overlapping fields in relation to Figure 10a the melting pool boundaries are presented using curves with dashed lines. The microstructure of the slowly cooled regions, (Zone II) in Figure 10c,d, is characterized by large equiaxed grains with appreciable grain boundary areas. The grain boundary areas act as new nucleation sites for the next layer, and influence the crystallographic orientation of the growing grains in *z*-direction, as demonstrated in Figure 10d. Horizontal dashed line represents the border line between two successive deposited layers. Figure 10d demonstrates further the influence of the equiaxed structure in the n layer on the grain orientation and growth direction of the $n + 1$ layer. Equiaxed grain, indicated as point 1 in Figure 10c,d, is characterized with larger dendrites as compared to its surrounding. Point 2 represents a columnar grain that is growing parallel to the building direction (*z*-direction). The rotated grains are indicated as points 3 and 4.

Figure 11 illustrates the influence of laser overlapping regions on the melt pool morphology with reference to the optical micrographs in Figures 7 and 9a. It can be concluded that horizontal and vertical laser interactions are more significant in the lower layers of the SLM-printed specimen and their amount decreases by increasing the number of deposited layers, because each new layer adds more heat to the structure by which the solidification rate becomes slower in the upper layers. However, somewhere in the center, the horizontal laser interactions become more dominant and thus deposited layers can be recognized by the periodic and wavy borderlines as could be seen in Figure 9a. The vertical distance between these borderlines represent the layer thickness (40 µm) and the waviness represents the horizontal laser interactions.

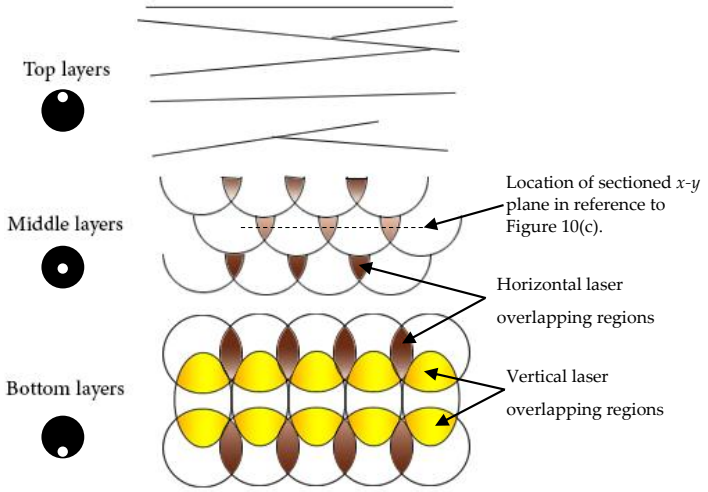

Figure 11. Illustration of vertical and horizontal laser overlapping and their influence on the melt pool morphology.

Figure 12 is the SEM 3D-composite micrograph showing the microstructure of the SLM-printed specimen. Both *x*-*z* and *y*-*z* planes, which are parallel to the deposition direction, showed matrices of γ''-phase and most probably MC-type carbide precipitates confined inside each columnar grain with elongated and equiaxed cellular substructures. Whereas, the *x*-*y* plane shows mainly equiaxed cellular substructures. The formation of these cellular substructures occur due to the high cooling rates during the SLM process [15] that are ranging between 10^5 and 10^8 °C/s [32,33], depending on the material and processing parameters. However, the details of formation mechanisms of various morphological features resulting from the SLM process still require further research. The grain boundaries are highlighted and guided by arrows to make better visibility of microdendrites of different orientations.

The heat flux direction and laser gradients associated with the laser scans of SLM process are complex and affected by number of factors [15,34], and no quantification of the cooling rate per laser track could be found in the literature. It is of high importance to highlight the characteristics of thermal

regime and their influence on the microstructure and texture evolution of SLM manufactured parts. Therefore, the development of models describing temperature evolution during the manufacturing process will be a great asset for the production of repeatable and reliable SLM parts.

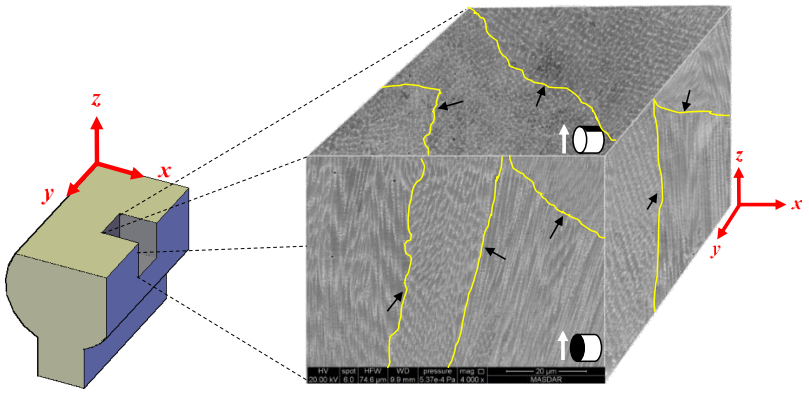

Figure 12. SEM 3D-composite micrograph showing the columnar structure of the SLM-printed cylinder with respect to the building direction. The black arrows are used to indicate the grain boundary lines.

3.1.3. Microstructure Evolution in Homogenized and HIP-Treated Specimens

When comparing both the SLM-printed and heat treated microstructures, the melting pool boundaries do not appear in the homogenized and HIP-treated specimens. However, both post-processing treatments showed common microstructural features. Numerous precipitates along grain boundaries were observed. The given numbers from 1 to 4 in Figures 13 and 14 correspond to γ-phase, δ-phase, MC-type carbide phase and γ''-phase, respectively, and their chemical analysis are discussed in Section 3.2.

Figure 13 illustrates the different microstructural features that were observed after 1 h holding at 1100 °C. Specifically, FEG-SEM examination showed that columnar grain structure has been altered and converted to a mixture of columnar and equiaxed grains as indicated in Figure 13a. Other complex grain geometries may result from grain boundary migration or sub-grain coalescence [35]. It is also worth noting that, the residual columnar grains became shorter after homogenization treatment and the grain size of the equiaxed structure is in the 30 to 50 µm (equivalent circle diameter) range. Such microstructural changes were presumed to occur due to the combination of nucleation and grain growth in the IN718 cast structures [26,36]. However, for the additive manufactured nickel alloys, Zhang et al. [37] described the homogenization kinetics based on the growth of the primary dendrites associated with rapid solidification of individual melt pool. They [37] further related the streaking patterns in homogenized structures to the elemental segregation in the fine columnar dendrites.

After homogenization treatment, different precipitates were residing at the grain boundaries as shown in Figure 13b. The needle-like and white precipitates, shown in Figure 13c,d, were recognized as δ-phase and MC-type carbides, respectively. Other fine precipitates, which correspond to γ''-phase, were dispersed within γ-phase matrix.

The microstructure of the HIP-treated IN718 alloy is shown in Figure 14, where more equiaxed grains and a higher volume fraction of carbide precipitates at the grain boundaries are present compared with the homogenized structure. An SEM image with high magnification is presented in Figure 14b to show the phase contents after HIP-treatment. Figure 14c,d are the high magnification SEM images showing δ-phase and carbide precipitates, respectively. It can be depicted from Figure 14c,d that γ'' precipitates are completely dissolved in the γ-phase matrix due to HIP-treatment as compared to the homogenized microstructure in Figure 13c,d. This is because the HIP treatment further exposed the material to high temperature, holding time and pressure thereby accelerating the γ''-phase dissolution [16]. Furthermore, the HIP-treated specimens were initially homogenized (i.e., the material encountered both heat treatments). Thus, it is expected to dissolve more γ''-phase during HIP-treatment.

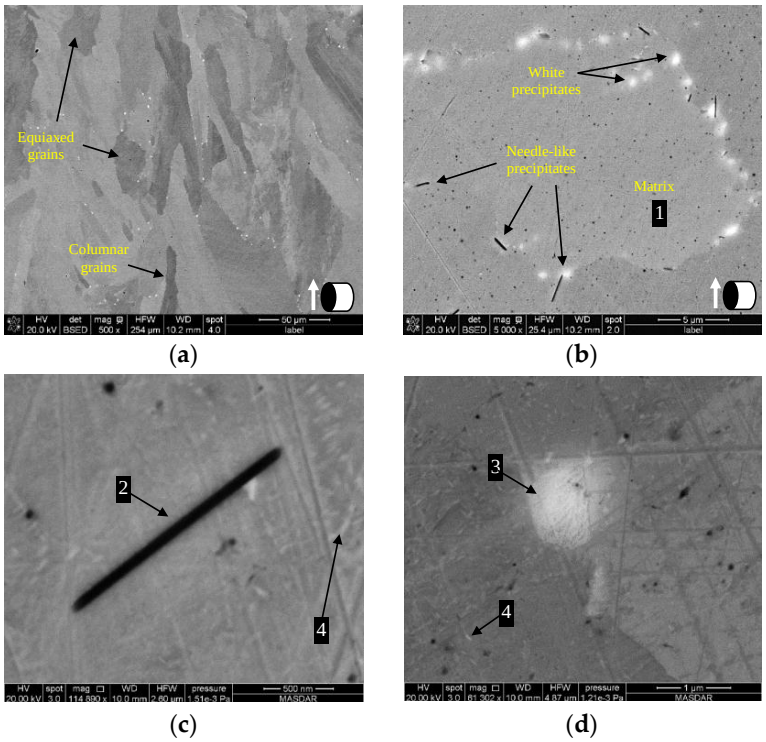

Figure 13. (**a**) Microstructure of a homogenized specimen; (**b**) different precipitates at the grain boundaries; (**c**,**d**) magnified images of δ-phase and MC-type carbide precipitates, respectively. The numbers correspond to the EDS spot analysis in Table 3.

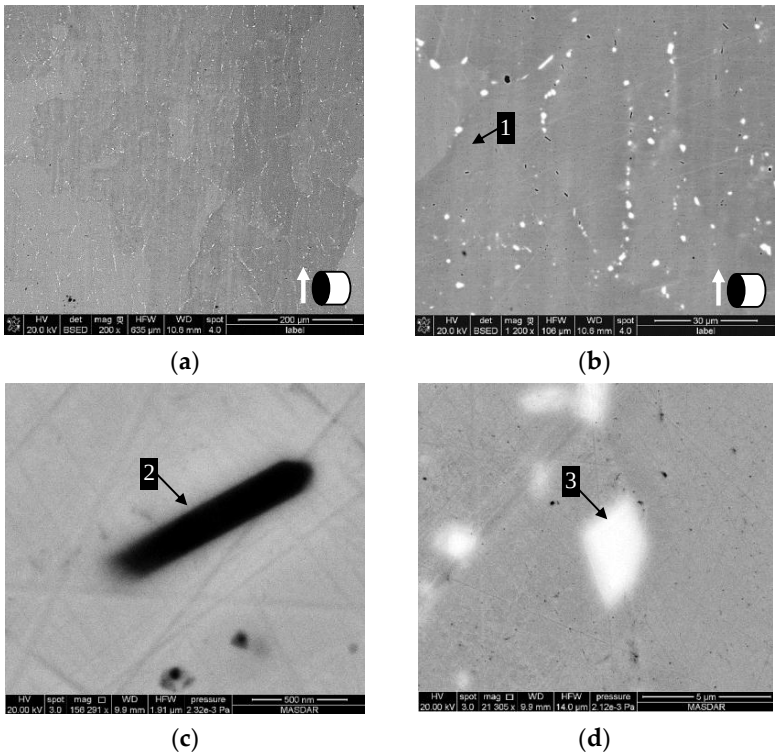

Figure 14. (**a**) Microstructure of hot isostatic pressing (HIP)-treated IN718 alloy; (**b**) magnified image showing the grain boundary precipitates after HIP-treatment; (**c**,**d**) enlarged images showing δ-phase and carbide phase, respectively. The numbers correspond to the EDS spot analysis in Table 3.

3.2. Phase Analysis of Heat Treated Specimens

The results of the EDS spot analysis of the matrix and different precipitates are given in Table 3. The spot numbers in Figures 13 and 14 correspond to those in Table 3. The elemental content of the matrix phase (spot 1) is almost the same as presented in Table 2, which was identified as γ-phase. The error of EDS measurements increases when analyzing small precipitates such as γ″ and δ-phase due to the volumetric interaction with the surrounding phases. Thus, the values are not absolute and regarded as semi-quantitative. EDS measurements were used to evaluate the detected phases in order to verify the XRD results and to compare with the available data from the literature. Table 3 shows that δ-phase contains higher Nb, Mo and Ti concentrations than those in the matrix. Similar microstructure was found in a solution treated SLM fabricated IN718 followed by a double aging treatment by Wang et al. [16] and was designated as δ-phase [38] with a rhombic crystal structure and Ni_3Nb formula. However, Wang et al. found the atomic ratio of Nb to Ni to be 1:1.77 (19.10 at % Nb and 33.86 at % Ni) [16], while in this study the ratio is equal to 1:4.17 with 8.75 at % Nb and 36.5 at % Ni. The high Nb to Ni ratio in this work may be due to the high Ni concentration acquired from the matrix phase, since the EDS spot diameter, with a special resolution of ~1 μm, is larger than the width of δ-phase needle. Nevertheless, the obtained Ni to Nb ratio in this work is acceptable, since it agrees with that reported by other authors with values ranging between 1:4.5 [39] and 1:2.85 [40].

The formation and changes in the δ-phase structure, as a result of several cooling and heating cycles during the AM process of ATI 718Plus nickel alloy, has been recently described by Idell et al. [41]. The high concentration of Nb, microsegregated at the interdendritic spaces of the dendritic microstructure, was found the reason for the δ-phase formation during solution treatment of the rapidly solidified Ni-based components. The Nb-rich regions in the microdendritic spaces contain γ″-phase, which was reported to undergo a phase transformation from bct-γ″ to orthorhombic δ-phase [42]. In the current work, the formation of δ-phase is in the same line as described by [41,42]. The Nb-rich regions in the interdendritic spaces of the powder and SLM-build specimens were observed in the EDS maps (Figure 5), and were recognized as γ″-phase using semi-quantitative EDS analysis, XRD refinement and literature data [4,17,28]. Homogenization treatment dissolved γ″-phase partially in the matrix and promoted the formation of ~35 nm thick and ~1000 nm long needle-like δ-phase precipitates. After HIP treatment, however, γ″ precipitates were completely dissolved and ~65 nm thick and ~650 nm long δ-phase needles were formed. The physical dimensions of δ-phase needles are consistent with those described by Idell et al. [41].

According to the transformation-time-temperature diagram of IN718 alloy (Figure 3), the dissolution temperature of δ-phase is about 1000 °C and therefore it is expected that all phase in the γ matrix be dissolved during the solution treatment. However, cooling the specimen in the furnace resulted in a very slow cooling rate of less than 2×10^{-3} °C/s, which can be represented as a linear function of temperature and time on Figure 3. The line intersects with δ-phase and γ″-phase fields at 1000 and 920 °C, respectively. Under these conditions, δ-phase forms first and probably continues to precipitate down to 750 °C. It is important to mention that no δ-phase could be found at the center of the SLM-printed specimens. This could be due to the high cooling rate during SLM fabrication (10^5–10^7 °C/s [15]), by which the slope of time-temperature line did not reach the formation boundaries of δ-phase. These microstructural observations are consistent with the precipitation-time-temperature diagram in Figure 3.

The chemical composition results further indicate that the white precipitates (spot 3) are enriched with Nb and Ti. These precipitates might be MC-type carbides [43], which were microstructurally associated with the δ-phase precipitates at the grain boundaries. This phase was surprisingly termed as Laves phase by [16,44]; however, it has different chemical composition than $(Ni,Cr,Fe)_2(Nb,Mo,Ti)$ as reported by [45–47]. Laves phase generally forms due to Nb segregation with other alloying elements, such as Ni, Cr and Fe, with a 1:2 ratio, which is different than MC-type carbide of nearly 1:1 ratio [18]. Differences between Laves and carbide phases in terms of composition and morphology were addressed by Parimi et al. [18]. In this work, Laves phase was not found within the microstructure

of the heat treated specimens. As suggested by [18,40], this can be attributed to the formation of grain boundary-type δ-phase below its solvus temperature of about 1000 °C and ageing time less than 100 h.

Table 3. EDS spot analysis of the homogenized IN718 specimen in at %.

Spot	Designation	Nb	Mo	Ti	Cr	Fe	Ni
1	γ-phase	3.96	1.67	1.47	22.4	19.65	49.85
2	δ-phase	8.75	8.25	12.70	18.65	15.15	36.50
3	MC-type carbide	77.50	-	22.50	-	-	-
4	γ″-phase	Below EDS detection limits [1]					

[1] EDS measurement error for each element is the same as in Table 2.

The driving force for carbide formation is the segregation of C and Nb when the alloy solidifies in the non-equilibrium condition [48]. The EDS analysis in Table 2 revealed that the Nb content varies from 4.73 at % in γ dendrites to 9.82 at % in γ″ precipitates for a quenched liquid microstructure in the GA powder. The SLM-printed microstructure, obtained in the rapidly cooled IN718 powder melt, contains γ″ precipitates with 3.43 at % Nb, dispersed in the γ matrix with ~1.46 at % Nb. The Nb concentration varies in the case of SLM-printed specimens due to the interaction of the EDS spot over very fine columnar dendritic architecture. The formation temperature of the carbide precipitates was recorded differently by several authors as 1250 °C [49], 1250–1255 °C [48], 1257 °C [50] and 1289 °C [51]. In the current work, the carbide precipitates were not positively detected in the SLM-printed specimens. It is possible that very fine carbides have been formed, but not detectable in the printed specimens, because of their size. However, after homogenization heat treatment the carbides grew by the diffusion process to have a complex morphology such that in Figures 13d and 14d. It might be possible to find differences in the carbide precipitation temperature due to the difference in the solidification rate, which greatly influences the chemical composition of the constituent phases [48]. The amount of these precipitates was found to increase after HIP-treatment as discussed in the following section.

Figure 15a,b shows the EDS spectrum acquired from δ-phase and MC-type carbides, respectively. The corresponding elemental maps are given in Figure 16, where the concentrations of Nb and Ti are higher in the carbide precipitates than in other phases. Similar MC-type carbide phase was reported by Sjoberg et al. [52] as (0.9Nb0.1Ti)C. Although δ-phase precipitates are very small in size, the elemental maps of Nb and Ti show noticeable contrast at their locations, indicating that these precipitates are enriched with these elements as compared to the matrix phase.

It was not possible to measure the chemical composition of γ″ precipitates, dispersed within γ-matrix, using EDS spot analysis. Their presence, however, was confirmed based on the high magnification SEM images in Figure 13c,d and X-ray diffraction patterns as will be discussed in Section 3.3.1.

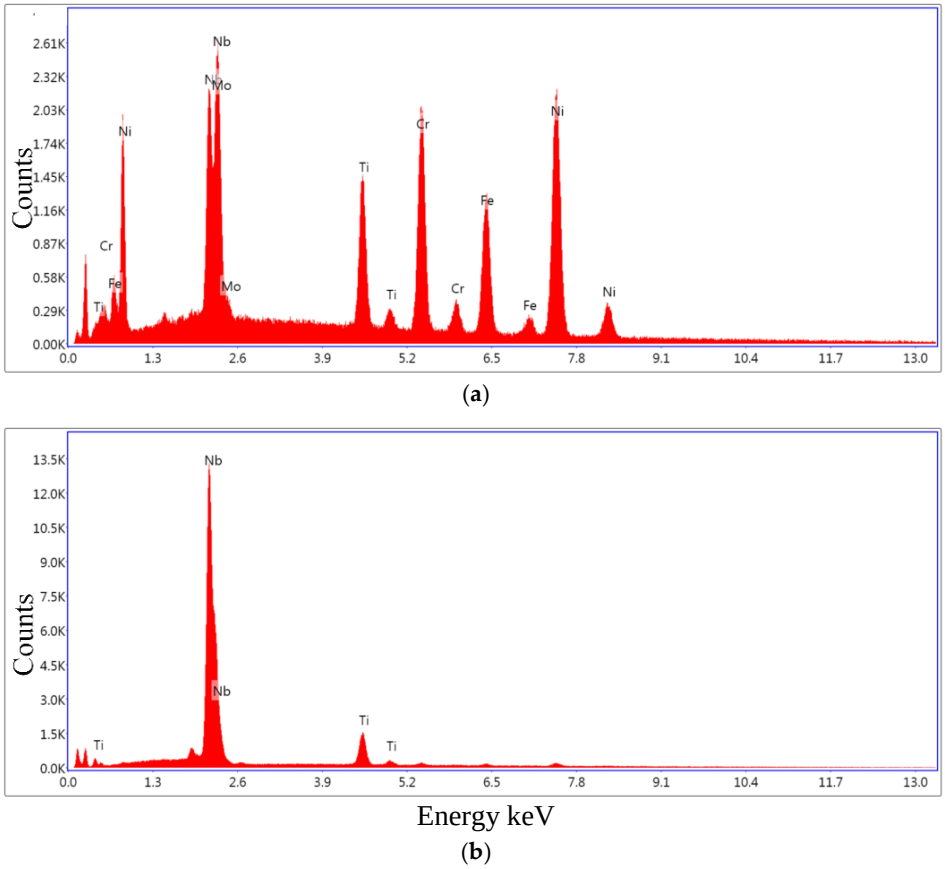

Figure 15. EDS spectra acquired from (**a**) δ-phase and (**b**) MC-type carbide phase.

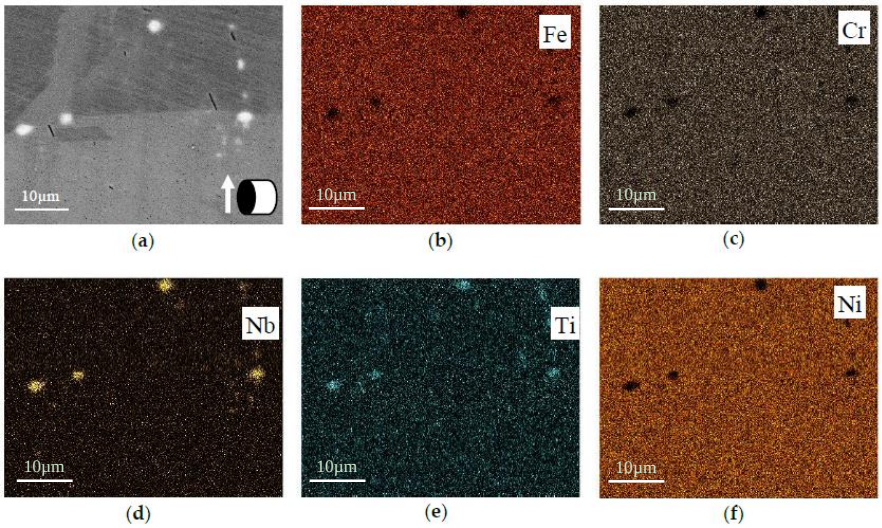

Figure 16. EDS elemental maps in the selected area (**a**) for Nb, Ti, Cr, Fe; and Ni (**b**–**f**), respectively.

3.3. Structure, Texture and Phase Evolution

3.3.1. Structure and Phase Analysis Using XRD

Figure 17 shows the XRD spectra of the as-printed, homogenized and HIP-treated specimens scanned across the base of the cylindrical specimens, as illustrated on the top right-hand corner. From the XRD results, two phases were positively identified in the SLM-printed specimen as γ-phase

and γ″-phase (bct-Ni_3Nb), which confirm the results obtained by EDS analysis. For the SLM-printed specimen, it is clear that the grains produce a dominant texture in the [002] direction. The texture in this direction is dictated by the columnar structure produced due to grain growth in the *z*-direction as discussed earlier in reference to Figure 9. The strong [002] texture in the SLM-fabricated IN718 was also reported by Amato et al. [17]. The diffraction peaks of γ″ precipitates overlap with [002], [022] and [113] peaks of the γ matrix. This demonstrates that the γ″ precipitates formed in a columnar microstructural architecture, parallel to the γ matrix, as could be seen in Figure 12.

With reference to microstructural analysis, the heat treatment processes reorganized the columnar architecture into equiaxed grains. Equally, the diffraction patterns of the homogenized and HIP-treated conditions, given in Figure 17, showed a dominant texture in [111] direction, which differs from that of the SLM-printed specimens. During the homogenization heat treatment, part of the columnar grains grow and change their orientation to form a texture in [111] direction, while the other grains remain in the [002] direction. More equiaxed grains formed after HIP-treatment, as could be inferred from Figure 14a, and thus the diffraction pattern shows a dominant texture in the [111], [222] and [022] directions.

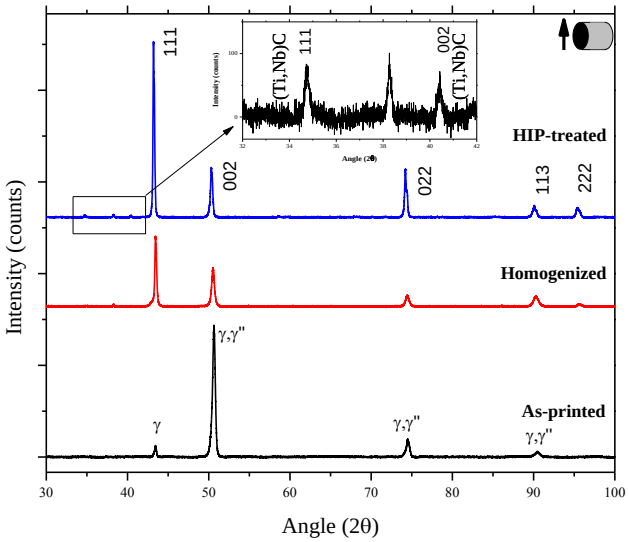

Figure 17. XRD spectra of as-printed, homogenized and HIP-treated specimens scanned in the vertical reference plane.

In compliance with EDS and microstructural analysis, the presence of δ-phase and carbide precipitates was confirmed by XRD analysis. Small quantities of the δ-phase precipitates formed upon homogenization treatment, as could be seen in the corresponding diffraction pattern as a small peak at 2θ = 38.2° (Figure 17). No remarkable change in the amount of the δ-phase precipitates could be noticed after HIP-treatment. This could be due to the non-uniform distribution of δ-phase as a result of variation in the cooling rate during SLM process. It might also be possible that δ-phase grew to the maximum volume fraction during homogenization treatment [41]. In contrast, the diffraction peaks of carbide precipitates were not detected after homogenization treatment due to their small quantities. However, their amount increased significantly after HIP treatment and their diffraction peaks were identified as shown in the enlarged spectrum in Figure 17. It has been reported that γ matrix dissolves γ″ precipitates upon HIP treatment at 1120 °C [4] and 1163 °C [17] for 4 h. Thus, the amount of carbide precipitates increased due to diffusion of the solute Ti and Nb, which partition in the matrix, towards the grain boundaries as a function of temperature. Summary of the identified phases in the current study and their crystallographic data, in comparison with the available information, is reported in Table 4. The crystal structure and lattice parameters of δ-phase were taken from [17], because the representative peaks of δ-phase in this work are very small.

Table 4. Identification and crystallographic data of the detected phases in the current study.

Phase	Crystal Structure	Prototype	Space Group	Lattice Parameters Å			Refs.
				a	*b*	*c*	
γ-phase	fcc	Cu	*Fm-3m*	3.60 (0) 3.59 3.59	-	-	This work [17] [4,28]
γ″-phase	bct	$TiAl_3$	*I4/mmm*	3.60 (9) 3.62 3.62	-	7.22 (4) 7.41 7.41	This work [17] [4,28]
δ-phase	orthorhombic	-	*Pmmm*	5.10	4.20	4.50	[17]
MC-type carbide $(Nb_{0.78}Ti_{0.22})C$	fcc	NaCl	*Fm-3m*	4.46 (7)	-	-	This work

3.3.2. Texture Evolution through 3D Printing and Heat Treatments

EBSD mapping was performed across the base of the printed cylinders (*x*-*z* plane), covering an area of about 800 μm × 700 μm at the center of the circle. The results reveal grain size and crystallographic texture differences between the SLM-printed, homogenized and HIP-treated specimens as demonstrated in Figure 18.

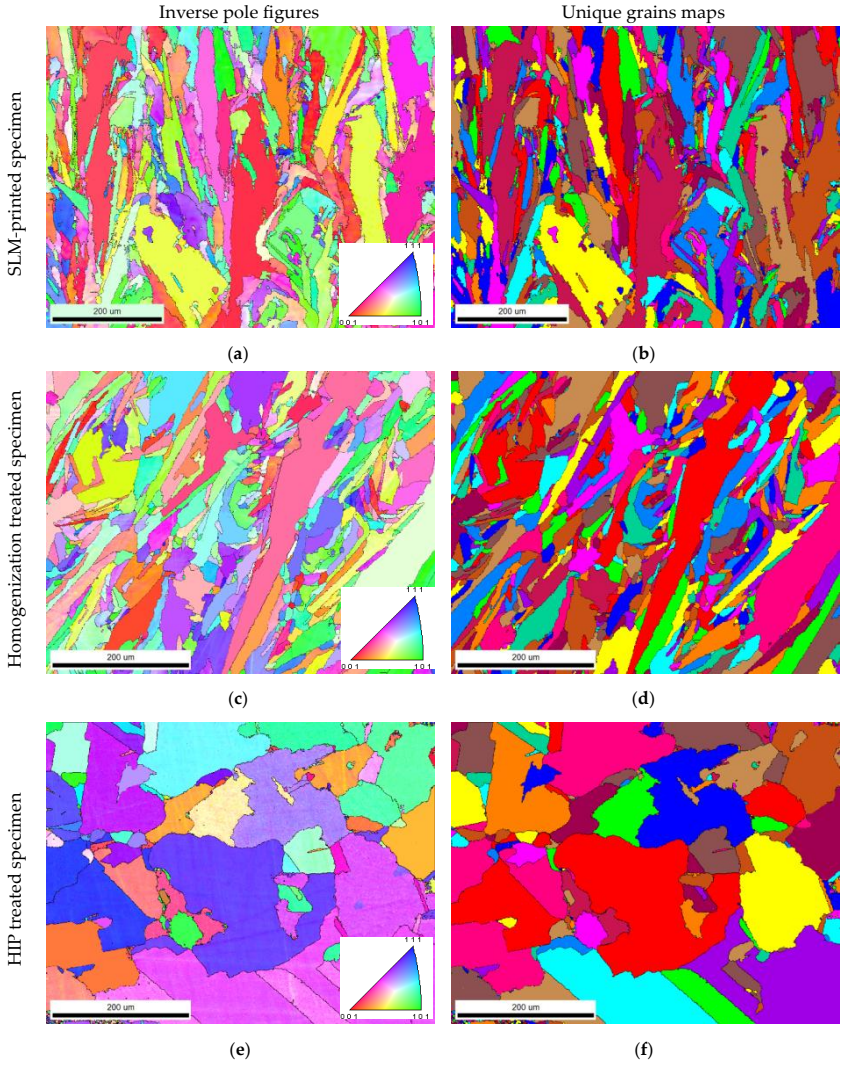

Figure 18. Inverse pole figures and unique grain maps of (**a**,**b**) SLM-printed; (**c**,**d**) homogenized; (**e**,**f**) HIP-treated IN718 specimens.

In agreement with XRD findings, the grain structure in the as-printed specimens, Figure 18a, showed columnar grains with (001) texture oriented in the building direction. EBSD maps further revealed that the grains' substructure observed in Figure 9b have the same orientation. The columnar grains, captured in the scanned area of the SLM-printed specimens, have an average size of about 300 μm × 50 μm as could be read from Figure 18b. This value is about 50% higher than those obtained after the homogenization heat treatment, as shown in Figure 18c,d. This structure was obtained after homogenization treatment (1100 °C for 1 h and furnace cooling), by which the columnar structure (fine grain bands) collapsed and smaller grains with random orientations developed. Both the SLM-printed and homogenized specimens show columnar-to-equiaxed grain transition with different percentages. For instance, the structure of the SLM-printed specimens contains more than 35% of columnar grains with an aspect ratio of about 4 as compared to 14% in the homogenized structure and about 30% of small grains with an aspect ratio of 2 as compared to 35% in the homogenized structure. HIP-treated specimen, as shown in Figure 18e,f, have more random textures with equiaxed morphologies. The average size of the equiaxed grains after HIP treatment (~150 μm equivalent circle diameter) is larger than those observed after homogenization (~50 μm).

3.3.3. Phase Evolution in SLM 3D Printed IN718 Alloys

Understanding the solidification behavior of the IN718 alloy is a key to know the phase evolution in the SLM-printed and heat treated conditions [48,50,51]. According to Murata et al. [51], the solidification sequence of IN718 alloy, with respect to temperature, starts with L → γ reaction (1359 °C) followed by the L → γ + MC-type carbide eutectic reaction that occurs at 1289 °C. The liquid phase terminates at 1160 °C, at which Laves phase forms. The δ-phase precipitates were found to form based on solid state reaction at 1145 ± 5 °C and both γ″ and γ′ precipitate at 1000 ± 20 °C. The observed microstructural evolution due to SLM process and the homogenization and HIP treatments in this work is represented in Figure 19.

The phase formation and decomposition mechanisms are generally governed by diffusion process [53], which is a strong function of concentration, time and temperature. Therefore, the post-processing treatments gave the driving force for the diffusing atoms in a supersaturated solid solution to precipitate the thermodynamic stable δ-phase, and simultaneously decompose the metastable γ″-phase. No remarkable change in the δ-phase amount could be noticed after the homogenization followed by HIP-treatment processes. This is an indication that as long as δ-phase forms due to the homogenization heat treatment, it stays stable during the HIP treatment. Generally, γ″ transforms to δ-phase [42], as discussed earlier, when Cr and Mo diffuse out from bct-γ″ to form orthorhombic-δ. In this work, both homogenization and HIP-treatments dissolve γ″-phase to a certain degree. No experimental evidence of the Laves phase presence was found in all specimens. Laves phase is normally irregular in shape and forms as a result of Nb segregation with other alloying elements [18]. Thus, the absence of Laves phase in the current work might be due to the high cooling rate during SLM process [54] induced in the investigated area.

On the basis of the observations and analysis of the results obtained in the present investigation the evolution of the phases in the SLM process can be summarized as the following: the SLM process changed the γ + γ″ + other secondary precipitates microstructure from a large dendritic in the gas atomized IN718 powder to a columnar structure. The homogenization treatment reoriented the columnar grains and provided the driving force for partial dissolution of γ″ in the matrix phase and precipitated grain boundary type δ-phase. Furthermore, both homogenization and HIP-treatments promoted the nucleation and growth of MC-type carbides at grain boundaries.

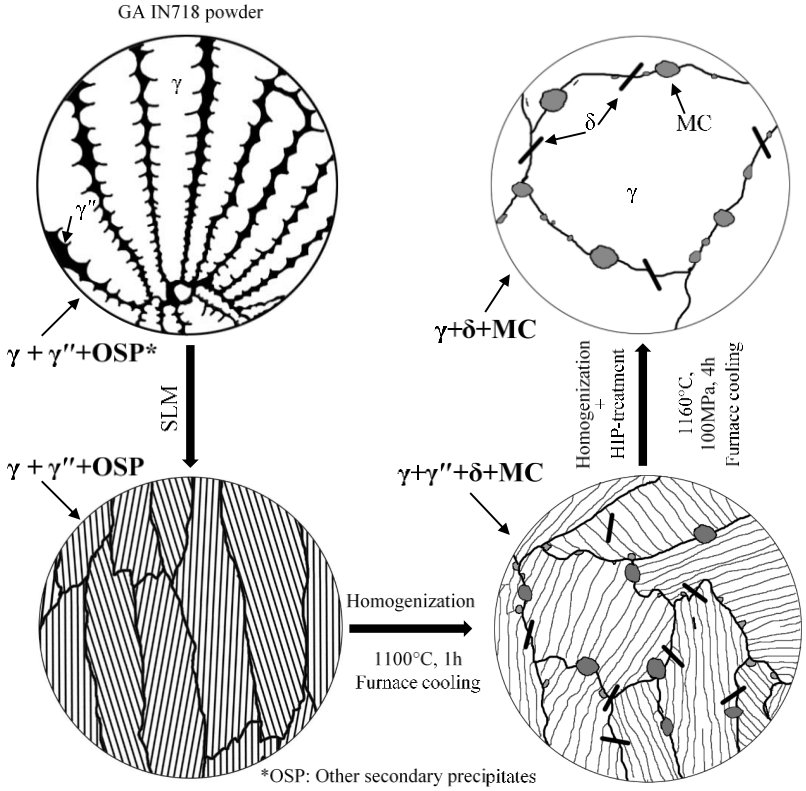

Figure 19. Schematic illustration of the microstructural changes and phase evolution in the gas atomized, 3D printed by SLM and heat treated IN718 superalloy.

4. Conclusions

The structure, texture and phase evolution of SLM-printed and heat treated IN718 superalloy were investigated and discussed. The powder-bed SLM additive manufacturing of pre-alloyed IN718 gas atomized powder produced nearly fully-dense IN718 cylindrical specimens. However, a steep thermal gradient between the initially and lastly deposited layers was captured based on the liquid melt pool morphology. The Gaussian shape of the melt pool in the lower layer was indicative of high cooling rate; whereas, the successive layers flatten progressively due to numerous reheating cycles by depositing and remelting new layers over the old ones.

The *x*-*z* and *y*-*z* planes of the SLM-printed specimens showed columnar grains of a strong {001} texture with fine elongated and equiaxed cellular substructures as a result of heat dissipation in negative *z*-axis. On the other hand, the *x*-*y* plane showed a unique periodic morphology, resulted from the laser beam overlapping (double-pass regions), that is mainly characterized by larger equiaxed grains and dendritic arm spacing as compared to the structure of single-pass regions. The laser overlapping regions further showed rotated grains that are almost perpendicular to the SLM building direction.

After thermal treatments, the area fraction of equiaxed grains increased from 20% to 100% through nucleation and grain growth. The post-processing treatments also provided the driving force for $\gamma'' \rightarrow \delta$ phase transformation and enhanced the nucleation and growth of MC-type carbides. The observed needle-like morphology of the δ-phase is an evidence that it is a grain boundary-type precipitate.

Acknowledgments: The authors thank Charles Simoneau and Karine Inaekyan for their assistance during the experimental work. Vladimir Brailovski and Mohammad Jahazi acknowledge the funds received from NSERC Discovery Grants to partially support this work. Vladimir Brailovski acknowledges the funds he received from ÉTS Research Chair for Additive Manufacturing Process Engineering, Materials and Structures. Mamoun Medraj acknowledges the funds received from Masdar Institute to carry out this research.

Author Contributions: Mamoun Medraj, Vladimir Brailovski and Mohammad Jahazi conceived and designed the SLM experiments and the microscopic analysis; Ahmad Mostafa and Ignacio Picazo Rubio performed the experiments; Ahmad Mostafa, Ignacio Picazo Rubio and Mamoun Medraj analyzed the data; Vladimir Brailovski and Mohammad Jahazi provided the 3D printing tools and post-treatments facilities; Ahmad Mostafa, Ignacio Picazo Rubio and Mamoun Medraj performed the sample characterization; Ahmad Mostafa and Ignacio Picazo Rubio wrote the paper; Vladimir Brailovski, Mohammad Jahazi and Mamoun Medraj revised the paper; Ahmad Mostafa and Mamoun Medraj improved the paper based on the reviewers comments and presented it in the current form.

Conflicts of Interest: The authors declare no conflict of interest.

References

1. Pacurar, R.; Pacurar, A. Applications of the selective laser melting technology in the industrial and medical fields. In *New Trends in 3D Printing*; Shishkovsky, I.V., Ed.; INTECH: Rijeka, Croatia, 2016. [CrossRef]
2. Wang, X.; Gong, X.; Chou, K. Review on powder-bed laser additive manufacturing of Inconel 718 parts. In Proceedings of the ASME 2015 International Manufacturing Science and Engineering Conference, Charlotte, NC, USA, 8–12 June 2015. [CrossRef]
3. Eisenhut, M.; Langefeld, B. *Additive Manufacturing: A Game Changer for the Manufacturing Industry*; Roland Berger Strategy Consultants GmbH: Munich, Germany, 2013.
4. Murr, L.E.; Martinez, E.; Gaytan, S.M.; Ramirez, D.A.; Machado, B.I.; Shindo, P.W.; Martinez, J.L.; Medina, F.; Wooten, J.; Ciscel, D.; et al. Microstructural architecture, microstructures, and mechanical properties for a nickel-base superalloy fabricated by electron beam melting. *Metall. Mater. Trans. A* **2011**, *42*, 3491–3508. [CrossRef]
5. Kistler, N.A. Characterization of Inconel 718 Fabricated through Powder Bed Fusion Additive Manufacturing. Bachelor's Thesis, The Pennsylvania State University, University Park, PA, USA, 2015.
6. Prasad, K.; Sarkar, R.; Ghosal, P.; Kumar, V. Tensile deformation behavior of forged disc of IN718 superalloy at 650 °C. *Mater. Des.* **2010**, *31*, 4502–4507. [CrossRef]
7. Paul, C.P.; Ganesh, P.; Mishra, S.K.; Bhargava, P.; Negi, J.; Nath, A.K. Investigating laser rapid manufacturing for Inconel-625 components. *Opt. Laser Technol.* **2007**, *39*, 800–805. [CrossRef]
8. Ganesh, P.; Kaul, R.; Paul, C.P.; Tiwari, P.; Rai, S.K.; Prasad, R.C.; Kukreja, L.M. Fatigue and fracture toughness characteristics of laser rapid manufactured Inconel 625 structures. *Mater. Sci. Eng. A* **2010**, *527*, 7490–7497. [CrossRef]
9. Zhang, Y.N.; Cao, X.; Wanjara, P.; Medraj, M. Fiber laser deposition of Inconel 718 using powders. In Proceedings of the Materials Science and Technology (MS&T) 2013 Conference, Montreal, QC, Canada, 27–31 October 2013.
10. Mumtaz, K.; Hopkinson, N. Selective laser melting of Inconel 625 using pulse shaping. *Rapid Prototyp. J.* **2010**, *16*, 248–257. [CrossRef]
11. Abioye, T.E.; Folkes, J.; Clare, A.T. A parametric study of Inconel 625 wire laser deposition. *J. Mater. Process. Technol.* **2013**, *213*, 2145–2151. [CrossRef]
12. Dinda, G.P.; Dasgupta, A.K.; Mazumder, J. Laser aided direct metal deposition of Inconel 625 superalloy: Microstructural evolution and thermal stability. *Mater. Sci. Eng. A* **2009**, *509*, 98–104. [CrossRef]
13. Jia, Q.; Gu, D. Selective laser melting additive manufacturing of Inconel 718 superalloy parts: Densification, microstructure and properties. *J. Alloys Compd.* **2014**, *585*, 713–721. [CrossRef]
14. Trosch, T.; Strößner, J.; Völkl, R.; Glatzel, U. Microstructure and mechanical properties of selective laser melted Inconel 718 compared to forging and casting. *Mater. Lett.* **2016**, *164*, 428–431. [CrossRef]
15. Choi, J.-P.; Shin, G.-H.; Yang, S.; Yang, D.-Y.; Lee, J.-S.; Brochu, M.; Yu, J.-H. Densification and microstructural investigation of Inconel 718 parts fabricated by selective laser melting. *Powder Technol.* **2017**, *310*, 60–66. [CrossRef]
16. Wang, Z.; Guan, K.; Gao, M.; Li, X.; Chen, X.; Zeng, X. The microstructure and mechanical properties of deposited-IN718 by selective laser melting. *J. Alloys Compd.* **2012**, *513*, 518–523. [CrossRef]
17. Amato, K.N.; Gaytan, S.M.; Murr, L.E.; Martinez, E.; Shindo, P.W.; Hernandez, J.; Collins, S.; Medina, F. Microstructures and mechanical behavior of Inconel 718 fabricated by selective laser melting. *Acta Mater.* **2012**, *60*, 2229–2239. [CrossRef]

18. Parimi, L.L.; Ravi, G.A.; Clark, D.; Attallah, M.M. Microstructural and texture development in direct laser fabricated IN718. *Mater. Charact.* **2014**, *89*, 102–111. [CrossRef]
19. Wei, H.L.; Mazumder, J.; DebRoy, T. Evolution of solidification texture during additive manufacturing. *Sci. Rep.* **2015**, *5*, 16446. [CrossRef] [PubMed]
20. Blackwell, P.L. The mechanical and microstructural characteristics of laser-deposited IN718. *J. Mater. Process. Technol.* **2005**, *170*, 240–246. [CrossRef]
21. EOS Gmbh Electro Optical Systems. *EOS Nickelalloy in718 Datasheet*; EOS Gmbh Electro Optical Systems: Munich, Germany, 2014.
22. Smith, D.H.; Bicknell, J.; Jorgensen, L.; Patterson, B.M.; Cordes, N.L.; Tsukrov, I.; Knezevic, M. Microstructure and mechanical behavior of direct metal laser sintered Inconel alloy 718. *Mater. Charact.* **2016**, *113*, 1–9. [CrossRef]
23. Thompson, R.G.; Dobbs, J.; Mayo, D. The effect of heat treatment on microfissuring in alloy 718. *Weld J.* **1986**, *65*, 299–304.
24. *X'Pert HighScore Plus*, version 3.0.2; software for phase identification from powder diffraction data; PANalytical: Almelo, The Netherlands, 2011.
25. Pierre, V. *Pearson's Crystal Data, Crystal Structure Database for Inorganic Compounds (on CD-ROM)*; ASM International: Materials Park, OH, USA, 2010.
26. Zhang, S.; Zhao, D. *Aerospace Materials Handbook*; CRC Press: Boca Raton, FL, USA, 2013.
27. Mullis, A.M.; Farrell, L.; Cochrane, R.F.; Adkins, N.J. Estimation of cooling rates during close-coupled gas atomization using secondary dendrite arm spacing measurement. *Metall. Mater. Trans. B* **2013**, *44*, 992–999. [CrossRef]
28. Murr, L.E.; Martinez, E.; Amato, K.N.; Gaytan, S.M.; Hernandez, J.; Ramirez, D.A.; Shindo, P.W.; Medina, F.; Wicker, R.B. Fabrication of metal and alloy components by additive manufacturing: Examples of 3D materials science. *J. Mater. Res. Technol.* **2012**, *1*, 42–54. [CrossRef]
29. Amine, T.; Newkirk, J.W.; Liou, F. An investigation of the effect of direct metal deposition parameters on the characteristics of the deposited layers. *Case Stud. Ther. Eng.* **2014**, *3*, 21–34. [CrossRef]
30. Antonsson, T.; Fredriksson, H. The effect of cooling rate on the solidification of Inconel 718. *Metall. Mater. Trans. B* **2005**, *36*, 85–96. [CrossRef]
31. Vrancken, B.; Wauthlé, R.; Kruth, J.-P.; Humbeeck, J.V. Study of the influence of material properties on residual stress in selective laser melting. In Proceedings of the Solid Free Fabrication Symposium, KU Leuven, Austin, TX, USA, 2–14 August 2013; pp. 1–15.
32. Saeidi, K.; Gao, X.; Zhong, Y.; Shen, Z.J. Hardened austenite steel with columnar sub-grain structure formed by laser melting. *Mater. Sci. Eng. A* **2015**, *625*, 221–229. [CrossRef]
33. Zheng, L.; Liu, Y.; Sun, S.; Zhang, H. Selective laser melting of Al–8.5Fe–1.3V–1.7Si alloy: Investigation on the resultant microstructure and hardness. *Chin. J. Aeronaut.* **2015**, *28*, 564–569. [CrossRef]
34. Zhou, X.; Li, K.; Zhang, D.; Liu, X.; Ma, J.; Liu, W.; Shen, Z. Textures formed in a CoCrMo alloy by selective laser melting. *J. Alloys Compd.* **2015**, *631*, 153–164. [CrossRef]
35. Liu, F.; Lin, X.; Yang, G.; Song, M.; Chen, J.; Huang, W. Recrystallization and its influence on microstructures and mechanical properties of laser solid formed nickel base superalloy Inconel 718. *Rare Met.* **2011**, *30*, 433–438. [CrossRef]
36. Lewandowski, M.S.; Sahai, V.; Wilcox, R.C.; Matlock, C.A.; Overfelt, R.A. High temperature deformation of Inconel 718 castings. In *Superalloys 718, 625, 706 and Various. Dérivatives*; Loria, E.A., Ed.; TMS-AIME: Warrendale, PA, USA, 1994; pp. 345–354. [CrossRef]
37. Zhang, F.; Levine, L.E.; Allen, A.J.; Campbell, C.E.; Lass, E.A.; Cheruvathur, S.; Stoudt, M.R.; Williams, M.E.; Idell, Y. Homogenization kinetics of a nickel-based superalloy produced by powder bed fusion laser sintering. *Scr. Mater.* **2017**, *113*, 98–102. [CrossRef]
38. Sochalski-Kolbus, L.M.; Payzant, E.A.; Cornwell, P.A.; Watkins, T.R.; Babu, S.S.; Dehoff, R.R.; Lorenz, M.; Ovchinnikova, M.; Duty, C. Comparison of residual stresses in Inconel 718 simple parts made by electron beam melting and direct laser metal sintering. *Metall. Mater. Trans. A* **2015**, *46*, 1419–1432. [CrossRef]
39. Slama, C.; Servant, C.; Cizeron, G. Aging of the Inconel 718 alloy between 500 and 750 °C. *J. Mater. Res.* **2011**, *12*, 2298–2316. [CrossRef]
40. Azadian, S.; Wei, L.-Y.; Warren, R. Delta phase precipitation in Inconel 718. *Mater. Charact.* **2004**, *53*, 7–16. [CrossRef]

41. Idell, Y.; Levine, L.E.; Allen, A.J.; Zhang, F.; Campbell, C.E.; Olson, G.B.; Gong, J.; Snyder, D.R.; Deutchman, H.Z. Unexpected δ-phase formation in additive-manufactured Ni-based superalloy. *JOM* **2016**, *68*, 950–959. [CrossRef]
42. Jouiad, M.; Marin, E.; Devarapalli, R.S.; Cormier, J.; Ravaux, F.; Le Gall, C.; Franchet, J.M. Microstructure and mechanical properties evolutions of alloy 718 during isothermal and thermal cycling over-aging. *Mater. Des.* **2016**, *102*, 284–296. [CrossRef]
43. Rao, G.; Sankaranarayana, M.; Balasubramaniam, S. Hot isostatic pressing technology for defence and space applications. *Def. Sci. J.* **2012**, *62*, 73–80. [CrossRef]
44. Clark, D.; Bache, M.R.; Whittaker, M.T. Shaped metal deposition of a nickel alloy for aero engine applications. *J. Mater. Process. Technol.* **2008**, *203*, 439–448. [CrossRef]
45. Janaki Ram, G.D.; Venugopal Reddy, A.; Prasad Rao, K.; Reddy, G.M.; Sarin Sundar, J.K. Microstructure and tensile properties of Inconel 718 pulsed Nd-YAG laser welds. *J. Mater. Process. Technol.* **2005**, *167*, 73–82. [CrossRef]
46. Schirra, J.J.; Caless, R.H.; Hatala, R.W. The effect of laves phase on the mechanical properties of wrought and cast + HIP Inconel 718. In *Superalloys 718, 625, 706 and Various. Dérivatives*; Loria, E.A., Ed.; TMS-AIME: Warrendale, PA, USA, 1991; pp. 375–388. [CrossRef]
47. Qi, H.; Azer, M.; Ritter, A. Studies of standard heat treatment effects on microstructure and mechanical properties of laser net shape manufactured Inconel 718. *Metall. Mater. Trans. A* **2009**, *40*, 2410–2422. [CrossRef]
48. Mitchell, A.; Schmalz, A.J.; Schvezov, C.; Cockroft, S. The precipitation of primary carbides in alloy 718. In *Superalloys 718, 625 and Various Derivatives*; Loria, E.A., Ed.; TMS-AIME: Warrendale, PA, USA, 1994; pp. 65–78.
49. Bouse, G.K. Application of a modified phase diagram to the production of cast alloy 718 components. In *Superalloy 718–Metallurgy Application*; Loria, E.A., Ed.; TMS-AIME: Warrendale, PA, USA, 1989; pp. 69–79.
50. Cieslak, M.J.; Knorovsky, G.A.; Headley, T.J.; Romig, A.D.J. The solidification metallurgy of alloy 718 and other Nb-containing superalloys. *Superalloy* **1989**, *718*, 59–68.
51. Murata, Y.; Morinaga, M.; Yukawa, N.; Ogawa, H.; Kato, M. Solidification structures of Inconel 718 with microalloying elements. *Superalloys* **1994**, *718*, 81–88.
52. Sjoberg, G.; Ingesten, N.G.; Carlson, R.G. Grain boundary δ-phase morphologies, carbides and notch rupture sensitivity of cast alloy 718. *Superalloys* **1991**, *718*, 603–620. [CrossRef]
53. Lifshitz, I.M.; Slyozov, V.V. The kinetics of precipitation from supersaturated solid solutions. *J. Phys. Chem. Solids* **1961**, *19*, 35–50. [CrossRef]
54. Oradei-Basile, A.; Radavich, J.F. A current TTT diagram for wrought alloy 718. *Superalloys* **1991**, *718*, 325–335.

© 2017 by the authors. Licensee MDPI, Basel, Switzerland. This article is an open access article distributed under the terms and conditions of the Creative Commons Attribution (CC BY) license (http://creativecommons.org/licenses/by/4.0/).